Applied Catalysis B: Environmental 257 (2019) 117919

Contents lists available at ScienceDirect

Applied Catalysis B: Environmental

journal homepage: www.elsevier.com/locate/apcatb

Carbon quantum dots decorated $Ba_{0.5}Sr_{0.5}Co_{0.8}Fe_{0.2}O_{3-\delta}$ perovskite nanofibers for boosting oxygen evolution reaction

Geng Li[a], Shuen Hou[a,**], Liangqi Gui[a], Feilong Feng[a], Dingbin Zhang[a], Beibei He[a,b,*], Ling Zhao[a,b,*]

[a] Faculty of Materials Science and Chemistry, China University of Geosciences, Wuhan, 430074, China
[b] Zhejiang Institute, China University of Geosciences (Wuhan), Hangzhou, 311305, China

ARTICLE INFO

Keywords:
Oxygen evolution reaction
Perovskites
Carbon quantum dots
Synergistic effect
Hollow nanofibers

ABSTRACT

Perovskites are emerging as a new research frontier for oxygen evolution reaction (OER), however, their activity and durability are still far from desirable. Herein, we highlight a facile approach to boosting the perovskite electrocatalysis for OER by the coupling of carbon quantum dots (CQDs). The as-prepared CQDs decorated $Ba_{0.5}Sr_{0.5}Co_{0.8}Fe_{0.2}O_{3-\delta}$ -perovskite nanofibers (CQDs@BSCF-NFs) catalyst achieves a low overpotential of 0.35 V at 10 mA cm^{-2}, favorably outperforming the individual BSCF-NFs and the commercial IrO_2. The CQDs@BSCF-NFs catalyst demonstrates an outstanding current density of 140.8 mA cm^{-2} at a potential of 1.65 V *vs.* RHE, which is ~5 and 19 times higher than that of BSCF-NFs and IrO_2. This significantly enhanced activity is attributed to the enlarged specific surface area, the increased surface oxygen vacancies as well as the synergy between CQDs and BSCF. Moreover, the CQDs@BSCF-NFs catalyst also exhibits a high electrocatalytic stability for 10 h operation.

1. Introduction

As excessive depletion of fossil fuels will escalate the energy crisis, the pursuit of highly efficient and environmentally friendly energy conversion and storage devices is becoming more and more urgent. Electrochemical oxygen evolution reaction (OER) is the core process for many renewable energy devices [1–4]. Unfortunately, the OER is kinetically sluggish due to a complex four-electron transfer process, resulting in a large overpotential (η) to achieve the desirable current density. At present. the precious metal oxides, *e.g.* RuO_2 and IrO_2, are regarded as the state-of-the-art catalysts towards OER, however, their costliness and terrestrial scarcity largely hinder their widespread applications [5]. It is thus challenging to develop the cost-effective, efficient and robust catalysts for OER.

Numerous efforts have been devoted to exploring the high performance non-precious catalysts for OER, such as carbon based materials [6,7], oxides [8–11], and hydroxides [12–15]. Among these candidates, perovskite oxides have drawn public attention because of their unique 3d electronic structure and structure flexibility [16–29]. In 2011, Suntivich et al. [16] systematically studied a series of perovskite-type catalysts for OER. It was revealed that the e_g-filling (σ*-orbital occupation) of perovskite catalysts was a critical indicator for their OER activity. For example, $Ba_{0.5}Sr_{0.5}Co_{0.8}Fe_{0.2}O_{3-\delta}$ (BSCF) perovskite with an e_g of ~1.2 delivered a superior intrinsic OER activity in contrast to IrO_2 catalyst. Although self-reconstruction readily occurred on BSCF surface as a formation of Co-based oxy(hydroxide) layers during long-term operation, it could retain the bulk perovskite structure as well as the high OER activity [22]. Furthermore, the rational doping and defects engineering can tune the e_g filling of perovskites and finally optimize the OER electrocatalytic activity, such as $SrNb_{0.1}Co_{0.7}Fe_{0.2}O_{3-\delta}$ [30], $SrCo_{0.95}P_{0.05}O_{3-\delta}$ [31], $Ca_{0.9}Yb_{0.1}MnO_{3-\delta}$ [32], $BaCo_{0.7}Fe_{0.2}Sn_{0.1}O_{3-\delta}$ [33], and $SrFe_{0.9}Si_{0.1}O_{3-\delta}$ [34].

In spite of materials engineering, the OER activity of the traditional perovskite catalysts are still far from desirable due to their low surface area and inferior electronic conductivity. There are usually the following two approaches to promote the performance of perovskite catalysts. One is to create a larger active surface area through the architecture of nanostructures. Another way is to design a synergic hybrid catalysts consisting of perovskite and electrically conductive supports [35]. For instance, $Sm_{0.5}Sr_{0.5}CoO_{3-\delta}$ perovskite hollow nanofibers (SSC-HF) hybridized with 3D N-doped graphene (3DNG) exhibited an increased OER bifunctional activity in alkaline media, which was

* Corresponding authors at: Faculty of Materials Science and Chemistry, China University of Geosciences, Wuhan, 430074, China.
** Corresponding author.
E-mail addresses: shenhou@cug.edu.cn (S. Hou), babyfly@mail.ustc.edu.cn (B. He), zhaoling@cug.edu.cn (L. Zhao).

https://doi.org/10.1016/j.apcatb.2019.117919
Received 22 April 2019; Received in revised form 30 June 2019; Accepted 4 July 2019
Available online 05 July 2019
0926-3373/

attributed to the electron transport from 3DNG to SSC-HF [36]. The similar synergistic effect was also confirmed in $(PrBa_{0.5}Sr_{0.5})_{0.95}Co_{1.5}Fe_{0.5}O_{5+\delta}$ (PBSCF) and 3DNG hybrid [37]. Chen et al. [38] proposed a core-corona structured catalyst consisting of $LaNiO_3$ core covered by porous nitrogen-doped carbon nanotube (NCNT) shell for oxygen electrocatalysis. Thanks to the high activity of the individual components and the biphase synergistic effect, such $LaNiO_3$-NCNT hybrid catalyst displayed an excellent charge and discharge performance in Zn-air batteries.

Recently, carbon quantum dots (CQDs) has emerged as a new generation carbon nanomaterials with small sizes (< 10 nm) because of its high surface area, rapid electron transfer, strong adhesion to catalyst, and environmental stability [39–41]. The cooperation of CQDs can contribute to overcoming the intrinsic limitations of perovskites, *e.g.* low surface area and inferior electron transfer process. Inspired by this concept, we highlighted a new type of CQDs decorated BSCF perovskite nanofibers (CQDs@BSCF-NFs) for efficiently electro-catalyzing OER. A facile two-step method of electrospinning and electrophoresis was applied to prepare the CQDs@BSCF-NFs catalyst. This hybrid catalyst demonstrated a remarkable high OER activity with a low overpotential of 0.35 V at 10 mA cm^{-2} and a good stability in alkaline media, which was superior to the individual BSCF and IrO_2 catalysts. The enlarged specific surface area, the increased surface oxygen vacancies, together with the synergistic effect between CQDs and BSCF contributed to the high electrocatalytic activity.

2. Experimental

2.1. Sample synthesis

2.1.1. Synthesis of BSCF-NFs

The BSCF-NFs were prepared by a facile electrospinning technique [42]. In a typical electrospinning process, 1 g of polyacrylonitrile (PAN) and the stoichiometric amount of $Ba(CH_3COO)_2$, $Sr(NO_3)_2$, $Co(NO_3)_3{\cdot}6H_2O$ and $Fe(NO_3)_3{\cdot}9H_2O$ were dissolved in 10 mL *N,N*-dimethylformamide (DMF) at room temperature. After intensely stirring for overnight, the resulting homogeneous solution was transferred into a plastic syringe equipped with a needle tip. The primary nanofibers were obtained by electrospinning at the applied voltage of 20 kV. The distance between tip and collector was about 20 cm, and the syringe feeding speed was 0.1 mL h^{-1}. The as-spun BSCF–PAN composite nanofibers were dried in an oven at 60 °C overnight, followed by rapid sintering at 1000 °C for 10 min. in air to prepare BSCF-NFs.

2.1.2. Synthesis of CQDs

The graphene oxides (GO) were prepared *via* a modified Hummers method [43]. Then, the CQDs were synthesized by a hydrothermal process. 150 mg of the as-prepared graphene oxides were dispersed in 20 mL of *N,N*-DMF, followed by ultrasonic processing for 0.5 h. Such mixture was transferred into a 30 mL Teflon-lined hydrothermal reactor and was heat-treated at 200 °C for 8 h. Subsequently, the mixture was filtered by using a 0.22 μm microporous membrane to obtain CQDs in DMF solution. The DMF was removed in a rotary evaporator at 80 °C. The remaining CQDs were dispersed in H_2O to form a CQDs aqueous solution.

2.1.3. Synthesis of CQDs@BSCF-NFs

CQDs@BSCF-NFs were synthesized in the assistance of a facile electrophoresis approach [44]. The as-prepared BSCF-NFs were dispersed into ethanol to form a suspension solution, which was evenly coated on Ni foams and was dried at 60 °C. The Ni foams supported BSCF-NFs was applied as the working electrode, and Pt plate served as the counter electrode. Subsequently, CQDs particles were deposited on the BSCF-NFs surface by an electrophoresis process at constant direct voltage of 6 V for 0.5 h. After ultrasonic stripping from the Ni foams, CQDs@BSCF-NFs was annealed in Ar at 200 °C for 0.5 h to achieve good structure stability.

2.1.4. Synthesis of BSCF bulk

BSCF bulk powders were prepared by a typical sol-gel method. Stoichiometric amount of $Ba(NO_3)_2$, $Sr(NO_3)_2$, $Co(NO_3)_3{\cdot}6H_2O$ and $Fe(NO_3)_3{\cdot}9H_2O$ were dissolved in the water, followed by the addition of chelating agents of EDTA and citric acid with the mole ratio of 1.5 (EDTA) : 1 (citric acid) : 1 (total metal ions). NH_4OH solution was gradually introduced until the pH value to ~9. Later, the resultant solution was heated on a hot plate till self-combustion occurred. Finally, the precursor were sintered at 1000 °C for 3 h to obtain BSCF bulk powders. In addition, the electrochemical performance of commercial IrO_2 (Sigma-Aldrich, 99.9%) were assessed for comparison.

2.2. Characterization

X-ray diffraction (XRD) of the as-synthesized catalysts were characterized by using a Bruker AXS D8-Focus diffractometer (Cu Kα radiation, λ = 0.15418 nm). Raman spectra were recorded on an HR 800 Raman spectroscope (Jobin Yvon) by using a synapse CCD detector together with a confocal Olympus microscope. Scanning electron microscope (FESEM SU8010) and transmission electron microscope (HRTEM Tecnai 20) equipped with Energy Dispersion Spectrum (EDS) were conducted to study the morphologies of catalysts. Electron paramagnetic resonance (EPR) spectra were collected on a Bruker EPR A300 spectrometer at room temperature. X-ray photoelectron spectra (XPS) were carried out *via* using a Kratos Axis Ultra DLD with the Al Kα excitation source. XPS data were calibrated by referencing C 1s to 284.8 eV, and then were analyzed based on XPSPEAK software. Specific surface areas of catalysts were performed by using a brunauer emmet teller (BET, TriStar II 3020), where nitrogen was applied as the adsorption source.

2.3. Electrochemical measurements

Electrochemical tests were performed in a typical three-electrode system by using an electrochemical station (Gamry, Interface 1000). A glassy carbon (GC) with 3 mm in diameter, a saturated calomel electrode (SCE), and a Pt plate served as the working electrode, the reference electrode, and the counter electrode, respectively. The catalysts were loaded on GC by drop casting way [45], generating a catalyst loading of 0.2264 mg_{cat} cm^{-2}. An O_2-saturated 1 M KOH alkaline solution was applied as the liquid electrolyte, which was purged with O_2 for 0.5 h prior to the electrochemical test and was continuously supplied during the testing procedure. The linear sweep voltammetry (LSV) with IR correction was conducted at a scan rate of 10 mV s^{-1} with the electrode rotation rate of 1600 rpm. Electrochemical impedance spectra (EIS) was performed at the potential of 1.60 V (*vs* RHE) with frequency ranging of 1 MHz–0.1 Hz. The chronopotentiometry was monitored under a constant potential of 10 mA cm^2 for OER to evaluate the long-term stability. All the measured potentials were calibrated to the reversible hydrogen electrode (RHE).

3. Results and discussion

3.1. Phase structure and morphology

The synthetic pathway for CQDs@BSCF-NFs hybrid catalyst is illustrated in Fig. 1a. Firstly, the nanofiber precursors were prepared *via* an electrospinning technology, followed by sintering at 1000 °C to form hollow BSCF-NFs. Subsequently, CQDs were deposited on BSCF-NFs surface by a facile electrophoresis method. The phase structure of the as-prepared nanofibers were identified by XRD and Raman. One can see that both BSCF bulk and BSCF-NFs show a cubic perovskite structure, and the perovskite structure remains stable after electrophoresis (Fig. 1b). Additionally, the characteristic peaks of carbon are hardly to

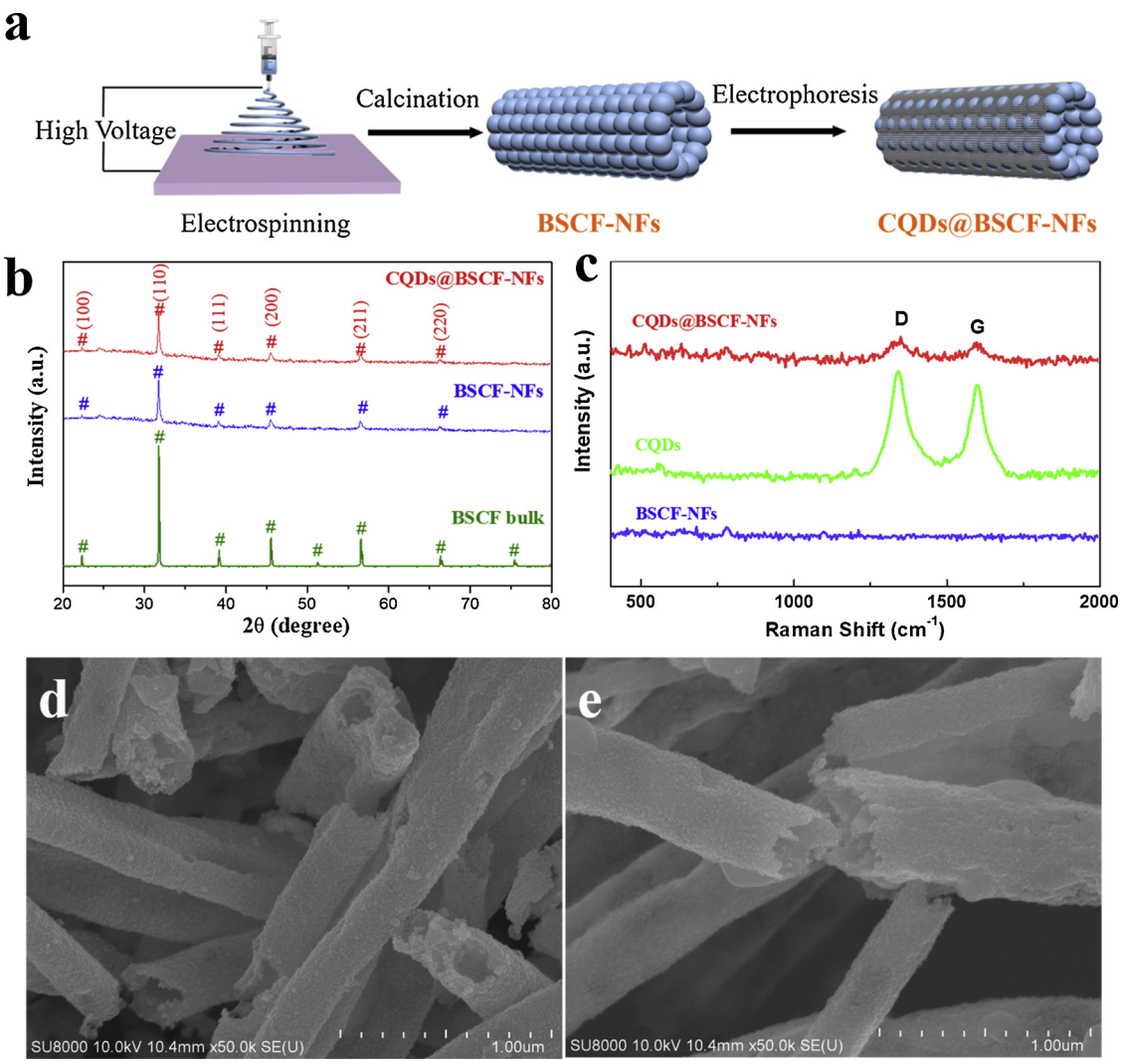

Fig. 1. (a) Scheme of the preparation pathway of CQDs@BSCF-NFs, (b) XRD patterns of the BSCF-bulk, BSCF-NFs and CQDs@BSCF-NFs samples, (c) Raman spectrogram of CQDs, BSCF-NFs and CQDs@BSCF-NFs samples, SEM images of (d) BSCF-NFs and (e) CQDs@BSCF-NFs samples.

be observed in CQDs@BSCF-NFs catalyst, probably due to the low amount and the relatively low diffraction intensity of CQDs. Fig. 1c presents the Raman spectrum of the pristine CQDs, BSCF-NFs, and CQDs@BSCF-NFs samples. A D-band at ~1360 cm^{-1} and a G band at ~1576 cm^{-1} are detected on CQDs and CQDs@BSCF-NFs samples, which are in good agreement with previous reported CQDs [46].

Fig. S1 presents the morphology of as-spun initial nanofibers before calcination. The surface of initial nanofibers are clean and smooth with an average diameter of ~200 nm, whereas a hollow structure (Fig. 1d) is obtained after calcination due to the Kirkendall effect [47]. On the other hand, the particles of BSCF bulk prepared by a sol-gel way are several microns and are severely agglomerated, as shown in Fig. S2. By comparison, the hollow structure ensures a large surface area and is conducive to electron and mass transportation. In the case of CQDs preparation, the well-dispersed CQDs particles with an average size of ~3 nm are obtained (Fig. S3). Moreover, there is no obvious change in the morphology of BSCF-NFs after CQDs modification (Fig. 1e). In order to gain an insight into the microstructure of CQDs@BSCF-NFs, HRTEM images are conducted and shown in Fig. 2. The measured *d* spacing values of 0.32 nm and 0.28 nm in Fig. 2b are well indexed to the (002) plane of CQDs and (110) plane of BSCF, respectively. The EDS mapping in Fig. 2c shows that the distribution of C element in the edge is slightly higher than that in the interior, denoting the successful deposition of CQDs on BSCF-NFs surface. The corresponding EDS mapping spectra of CQDs@BSCF-NFs sample are presented in Fig. S4.

3.2. OER performance

To evaluate the electrocatalytic OER performance, the as-prepared BSCF bulk, BSCF-NFs, CQDs@BSCF-NFs, and commercial IrO_2 catalysts were performed in 1 M KOH solution by using a standard three-electrode system. As shown in Fig. 3a, the BSCF bulk generates a current density of 10.5 mA cm^{-2} at a potential of 1.65 V *vs.* RHE, which is slightly higher than 7.2 mA cm^{-2} on IrO_2 catalyst. In Fig. S5, the specific activity of BSCF bulk is two orders of magnitude higher than that of commercial IrO_2, indicating that the BSCF perovskite is intrinsically active for OER. By nano-structural engineering, the BSCF-NFs exhibits a current density of 26.3 mA cm^{-2} at a potential of 1.65 V *vs.* RHE (Fig. 3a). Importantly, the CQDs@BSCF-NFs catalyst demonstrates a significantly enhanced current density of 140.8 mA cm^{-2} at a potential of 1.65 V *vs.* RHE, which is 13 and 5 times higher than that of BSCF bulk and BSCF-NFs, respectively. It is well accepted that the OER overpotential (η) at 10 mA cm^{-2} is an important index to assess the catalyst activity, according to a metric target for solar fuel synthesis [48]. The CQDs@BSCF-NFs catalyst delivers a η of only 0.35 V, which is lower than that of IrO_2 (0.44 V), BSCF bulk (0.42 V), and BSCF-NFs (0.37 V) catalysts (Fig. 3b). A comparison on the OER activity of the current catalysts and other state-of-the-art perovskite catalysts are illustrated in

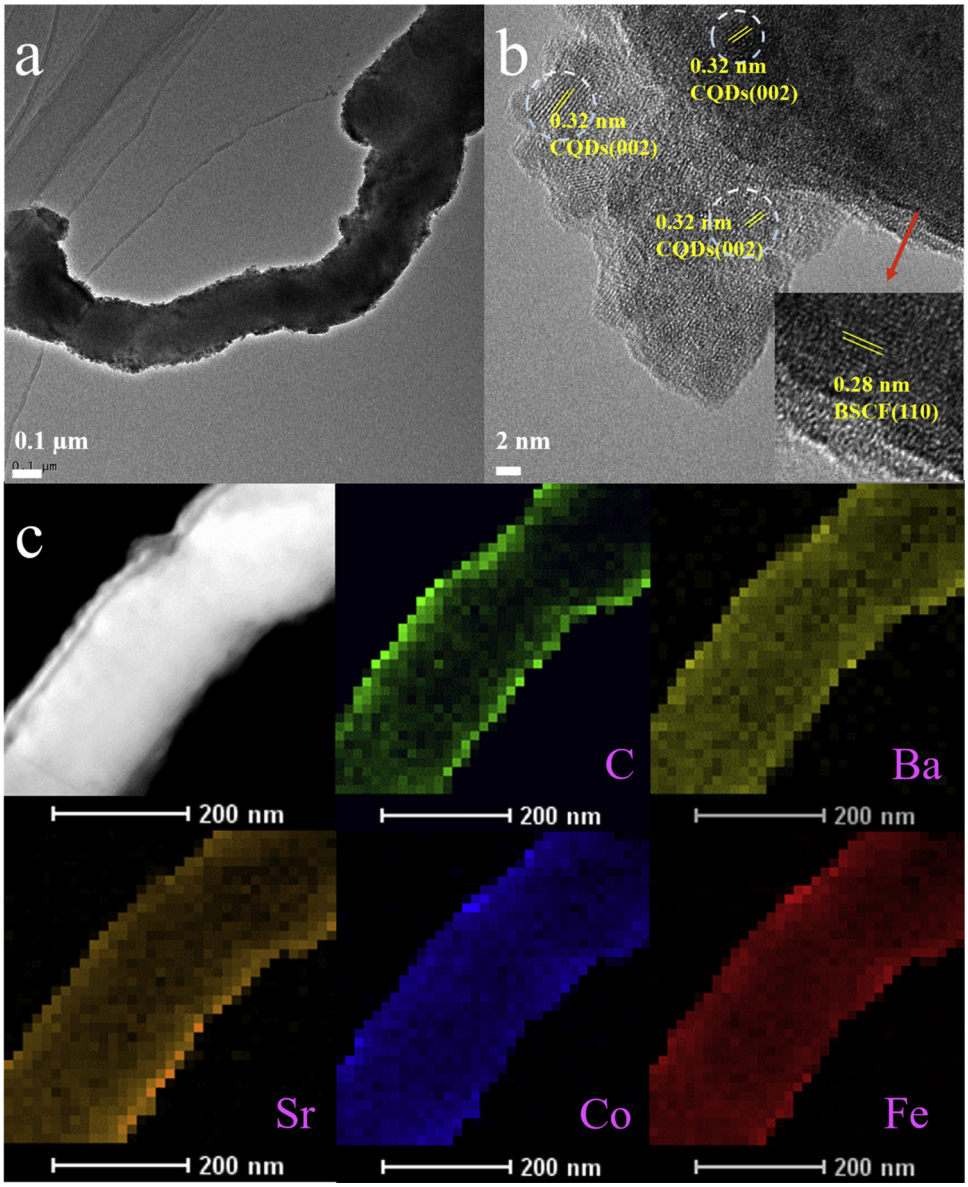

Fig. 2. (a) Low magnification, (b) High magnification TEM images, (c) HAADF-STEM and corresponding EDS element mapping of CQDs@BSCF-NFs catalyst.

Table 1. The LSV of CQDs@BSCF-NFs catalyst was also assessed in 0.1 M KOH electrolyte for comparison (Fig. S6). Of note, the OER performance, especially the current density, of CQDs@BSCF-NFs is favorably comparable to other excellent perovskite catalysts, indicating a superior OER activity of CQDs@BSCF-NFs catalyst.

The Tafel slope and EIS measurements of the as-prepared catalysts were further conducted to study their OER kinetics. The Tafel slope (Fig. 3c) of IrO_2, BSCF bulk, BSCF-NFs, and CQDs@BSCF-NFs catalysts is 106, 104, 103, 66 mV dec^{-1}, respectively. A similar trend is obtained for polarization resistance (Fig. 3d). The polarization resistance of IrO_2, BSCF bulk, BSCF-NFs, and CQDs@BSCF-NFs catalysts is approximately 151, 100, 46, and 23 Ω, respectively. The lowest Tafel slope together with the lowest polarization resistance indicate the fastest OER kinetics of CQDs@BSCF-NFs among these studied catalysts.

3.3. Role of CQDs

Understanding the role of CQDs on electrocatalytic performance can offer the guidelines to further design highly efficient catalysts for OER. The surface area is one of the key factors for catalysts. Fig. S7 shows the specific surface area of BSCF bulk, BSCF-NFs, and CQDs@BSCF-NFs catalysts. It is clear that the hollow nanofibers structure provides the significantly higher specific surface area than bulk sample. And, the introduction of CQDs can further enlarge the specific surface area. This enlarged specific surface area of CQDs@BSCF-NFs catalyst can ensure an increased electrocatalytic solid–electrolyte contact area for electrocatalytic reaction.

Fig. 4a presents the EPR spectra of BSCF-NFs and CQDs@BSCF-NFs catalysts. Both BSCF-NFs and CQDs@BSCF-NFs exhibit an EPR signal at g = 2.003, which corresponds to electrons trapped in oxygen vacancies [49]. The higher signal intensity on CQDs@BSCF-NFs sample denotes that CQDs@BSCF-NFs catalyst has more surface oxygen vacancies than the pristine BSCF-NFs catalyst. Fig. 4b displays the O 1s XPS spectra of BSCF-NFs and CQDs@BSCF-NFs catalysts, consisting of lattice oxygen O^{2-} (~528.8 eV), highly oxidative oxygen O_2^{2-}/O^- (~530.5 eV), hydroxyl groups or surface adsorbed oxygen −OH or O_2 (~531.5 eV), and adsorbed molecular water H_2O (~532.9 eV) [50]. The simulated relative concentration of those oxygen species are illustrated in Table S1. It has been reported that the O_2^{2-}/O^- species for perovskite oxides is closely related to the surface oxygen vacancies [51,52]. One can see

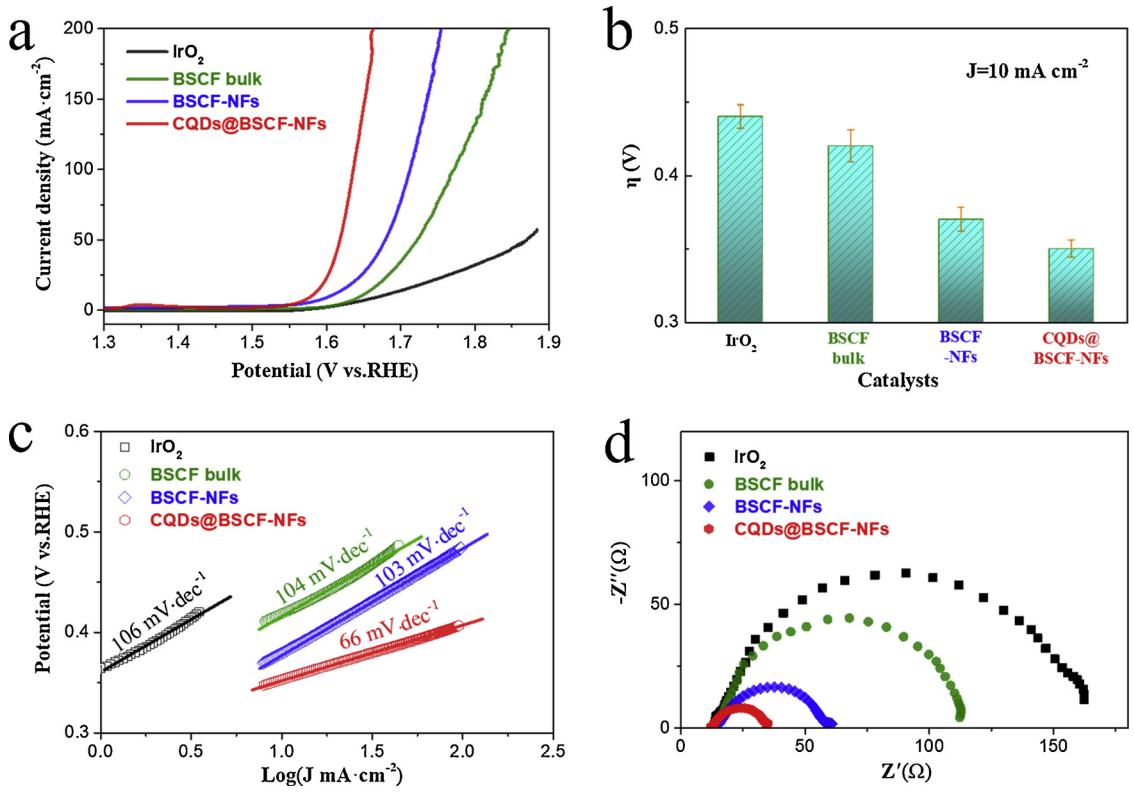

Fig. 3. (a) LSV curves, (b) Overpotential at currents densities of 10 mA cm^{-2} (Error bars derived from at least three independent measurements), (c) Tafel plots, (d) Nyquist curves of the IrO_2, BSCF-bulk, BSCF-NFs and CQDs@BSCF-NFs catalysts for OER in 1 M KOH alkaline solution.

that the introduction of CQDs can increase the concentration of O_2^{2-}/O^-, which is attributed to the partially reaction of lattice oxygen in BSCF with CQDs at 200 ℃ to as the formation of oxygen vacancies. These oxygen vacancies in catalyst surface prefer to provide connected channels for intermediate oxygen species, such as O_2 molecules, O^{2-} and OH^- ions [53]. It is revealed that the hydroxyl species (OH-) at the surface of catalyst can enhance the OER activity in an alkaline solution [54]. Therefore, the oxygen vacancies are electrochemically active for OER.

In the case of C 1s spectra, the signals of C—C at 284.8 eV, C–O at 286.5 eV, C═O at 287.9 eV, and O═C–O signal at 289.0 eV are obtained (Fig. 4c) [46]. In comparison to the pristine CQDs, the CQDs@BSCF-NFs catalyst has a relatively higher content of C/O bonds, implying that the CQDs and BSCF probably form a complex CQDs@BSCF-NFs by C/O bonds. In addition, the core-level spectra of Co 2p and Fe 2p of BSCF-NFs and CQDs@BSCF-NFs catalysts are shown in Fig. 4d and e. Compared to BSCF-NFs, the spectra of Co 2p and Fe 2p of CQDs@BSCF-NFs shift to the lower binding energies, suggesting the strong interaction between CQDs and BSCF as well. Compared with semi-conductive BSCF, electronic conductive CQDs has a higher Fermi level, implying the possible electron transfer from CQDs to BSCF and the transformation of Fermi level for BSCF (Fig. 4f). This synergistic effect between CQDs and BSCF can increase the covalency between transition metals and lattice oxygen, and consequently promote charge transfer between surface cations and adsorbates for boosting OER kinetics [37].

3.4. Stability

Besides the OER activity, the long-term durability is another vital criterion for the practical feasibility of catalysts. Accordingly, the prolonged chronopotentiometry curves of BSCF-NFs and CQDs@BSCF-NFs catalysts were performed at a current density of 10 mA cm^{-2} in 1 M KOH alkaline solution, as shown in Fig. 5a. After 10 h operation, BSCF-NFs catalyst displays a poor stability, the OER performance of which

Table 1
A comparison of the as-prepared catalysts and other state-of-the-art perovskite catalysts for OER.

Catalysts	Electrolyte	Catalyst loading (mg cm^{-2})	η(V)@10mA cm^{-2}	J(mA·cm^{-2})@1.65 V *vs.* RHE	Tafel slope (mV dec^{-1})
CQDs@BSCF-NFs (this work)	1 M KOH	0.23	0.35	140.8	66
CQDs@BSCF-NFs (this work)	0.1 M KOH	0.23	0.38	35	–
BSCF [30]	0.1 M KOH	0.23	0.51	~3	94
Ball-milled $SrNb_{0.1}Co_{0.7}Fe_{0.2}O_{3-\delta}$ [30]	0.1 M KOH	0.23	0.42	~10	90
$SrNb_{0.1}Co_{0.7}Fe_{0.2}O_{3-\delta}$ Nanorod [57]	1 M KOH	0.46	0.37	~55	48
$NdBaMn_2O_{5.5}$ [58]	1 M KOH	0.40	0.37	~12	75
La_2NiMnO_6 [25]	1 M KOH	–	0.37	~30	58
$(PrBa0.8Ca_{0.2})_{0.95}(Co_{1.5}Fe_{0.5})_{0.95}Co_{0.05}O_{5+\delta}$@$Co/CoO_x$ [59]	1 M KOH	0.20	0.38	~20	99
$La_{0.5}Sr_{0.5}MnO_{3-\delta}$-$Fe_3C$-Nitrogen-doped Carbons [60]	0.1 M KOH	0.27	0.37	~22	139
$La_{0.5}(Ba_{0.4}Sr_{0.4}Ca_{0.2})_{0.5}Co_{0.8}Fe_{0.2}O_{3-\delta}$/Reduced Graphene Oxide [61]	1 M KOH	0.50	0.31	~66	80
$Sm_{0.5}Sr_{0.5}CoO_{3-\delta}$-N-doped graphene [36]	0.1 M KOH	0.80	0.40	~15	115
$(PrBa_{0.5}Sr_{0.5})O_{0.95}Co_{1.5}Fe_{0.5}O_{5+\delta}$-N-doped graphene [37]	0.1 M KOH	0.80	0.32	–	74

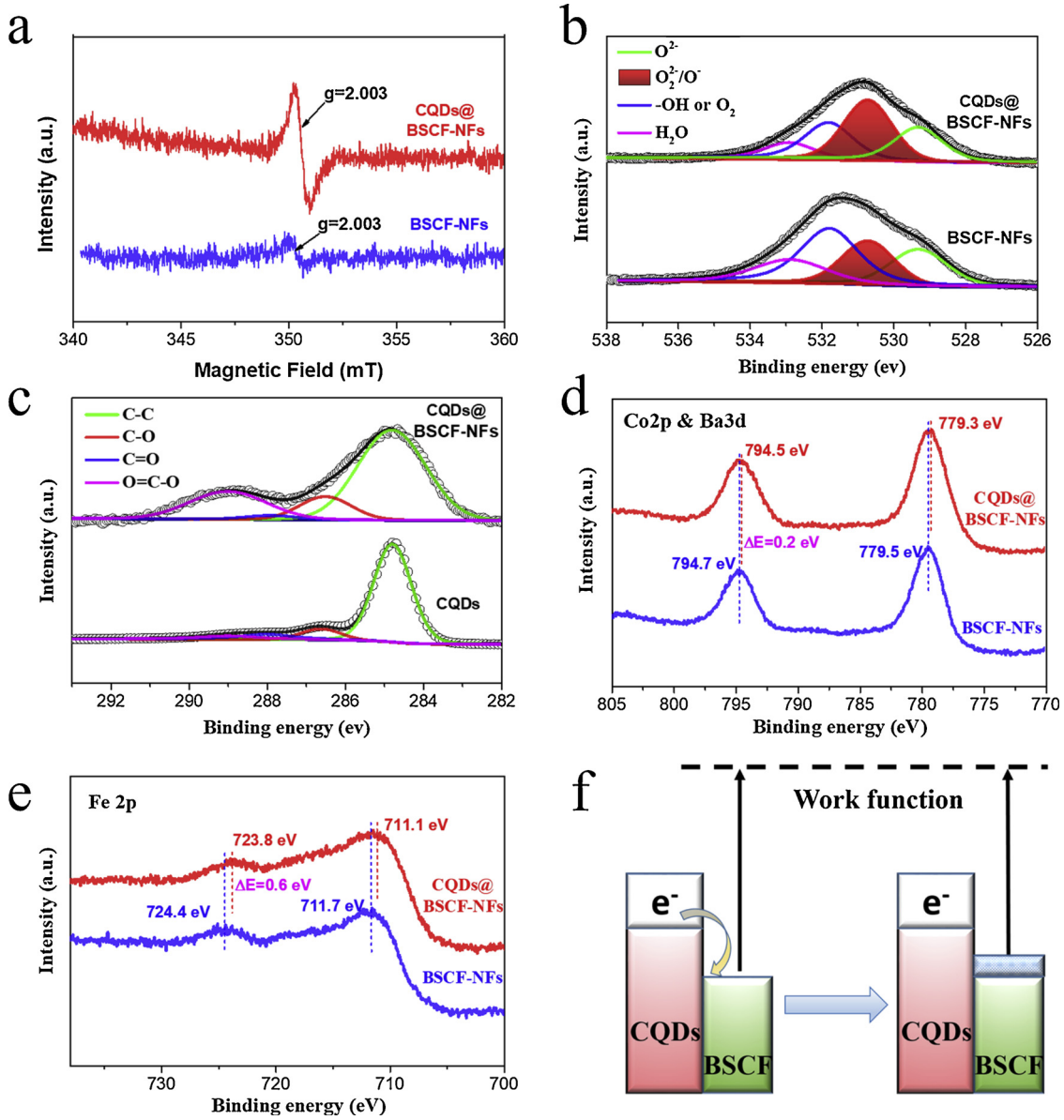

Fig. 4. (a) EPR spectra of BSCF-NFs and CQDs@BSCF-NFs, XPS spectra of (b) O 1s for BSCF-NFs and CQDs@BSCF-NFs, (c) C 1s for CQDs and CQDs@BSCF-NFs, (d) Co 2p @ Ba 3d and (e) Fe 2p species for BSCF-NFs and CQDs@BSCF-NFs, (f) Schematic of charge transfer between CQDs and BSCF perovskite.

decreases after the initial 2 h operation. By contrast, there is no obvious performance degradation on CQDs@BSCF-NFs catalyst during 10 h operation, indicating that the CQDs modification can improve the electrocatalytic stability of BSCF perovskite. Fig. 5b shows the HRTEM morphology of CQDs@BSCF-NFs catalyst after durability testing. After chronoamperometric measurement, the morphology of CQDs@BSCF-NFs is almost maintained. However, BSCF can preferentially self-reconstruct its surface, resulting in surface amorphous layer while retaining its perovskite structural in interior. Fig. 5c and 5d reveal that the high valence states of Co and Fe are obtained after long-term operation, indicating the amorphous layer is likely the formation of Co/Fe-based oxy(hydroxide) [22]. More importantly, this created Co/Fe-based oxy(hydroxide) layer is highly active for OER [55,56].

4. Conclusions

In summary, carbon quantum dots decorated $Ba_{0.5}Sr_{0.5}Co_{0.8}Fe_{0.2}O_{3-\delta}$ perovskite nanofibers (CQDs@BSCF-NFs) hybrid catalyst is fabricated by a two-step electrospinning and electrophoresis process. The surface modification of CQDs can not only increase the specific surface area and surface oxygen vacancies, but also promise the synergistic effect between BSCF and CQDs, which are beneficial for boosting the electrocatalytic activity towards OER. The newly designed catalyst demonstrates a remarkable electrocatalytic activity for OER with an overpotential of only 0.35 V at 10 mA cm^{-2} and an excellent current density of 140.8 mA cm^{-2} at 1.65 V *vs.* RHE, which is superior to those of BSCF and commercial IrO_2. Furthermore, a prolonged stability of BSCF perovskite is obtained after CQDs modification. The encouraging results provide a new avenue for developing cost-effective, highly efficient and robust hybrid catalysts for OER and other electrochemical applications.

Acknowledgements

The project was supported by the National Natural Science Foundation of China (Grant No. 51402266 and 21401171). The project was supported by the Natural Science Foundation of Zhejiang Province (Grant No. LY19E020001 and LY19B060003).

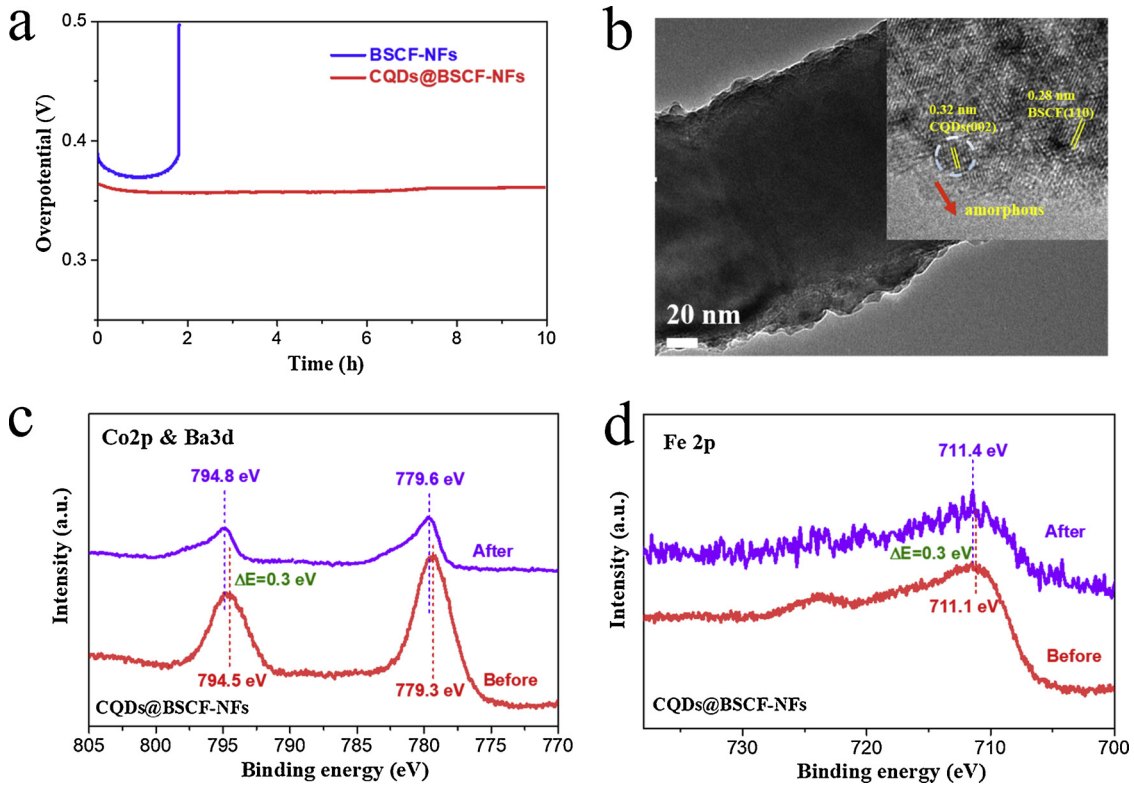

Fig. 5. (a) Chronopotentiometry curves of BSCF-NFs and CQDs@BSCF-NFs catalysts, (b) HRTEM image, XPS (c) Co 2p @ Ba 3d and (d) Fe 2p spectra of post-CQDs@BSCF-NFs.

Appendix A. Supplementary data

Supplementary material related to this article can be found, in the online version, at doi:https://doi.org/10.1016/j.apcatb.2019.117919.

References

[1] A. Muthurasu, V. Maruthapandian, H.Y. Kim, Metal-organic framework derived Co3O4/MoS2 heterostructure for efficient bifunctional electrocatalysts for oxygen evolution reaction and hydrogen evolution reaction, Appl. Catal. B-Environ. 248 (2019) 202–210.

[2] J.S. Kim, B. Kim, H. Kim, K. Kang, Recent progress on multimetal oxide catalysts for the oxygen evolution reaction, Adv. Energy Mater. 8 (2018) 1702774.

[3] G. Li, P.-Y.A. Chuang, Identifying the forefront of electrocatalytic oxygen evolution reaction: electronic double layer, Appl. Catal. B-Environ. 239 (2018) 425–432.

[4] X. Xu, W. Wang, W. Zhou, Z. Shao, Recent advances in novel nanostructuring methods of perovskite electrocatalysts for energy-related applications, Small Methods 2 (2018) 1800071.

[5] M.E.G. Lyons, F. Stephane, Mechanism of oxygen reactions at porous oxide electrodes. Part 2—oxygen evolution at RuO2, IrO2 and Ir(x)Ru(1-x)O2 electrodes in aqueous acid and alkaline solution, Phys. Chem. Chem. Phys. Pccp 13 (2011) 5314–5335.

[6] D.K. Singh, R.N. Jenjeti, S. Sampath, M. Eswaramoorthy, Two in one: N-doped tubular carbon nanostructure as an efficient metal-free dual electrocatalyst for hydrogen evolution and oxygen reduction reactions, J. Mater. Chem. A 5 (2017) 6025–6031.

[7] K. Mamtani, D. Jain, D. Dogu, V. Gustin, S. Gunduz, A.C. Co, U.S. Ozkan, Insights into oxygen reduction reaction (ORR) and oxygen evolution reaction (OER) active sites for nitrogen-doped carbon nanostructures (CNx) in acidic media, Appl. Catal. B-Environ. 220 (2018) 88–97.

[8] C. Li, B. Zhang, Y. Li, S. Hao, X. Cao, G. Yang, J. Wu, Y. Huang, Self-assembled Cu-Ni bimetal oxide 3D in-plane epitaxial structures for highly efficient oxygen evolution reaction, Appl. Catal. B-Environ. 244 (2019) 56–62.

[9] W.Q. Zaman, W. Sun, M. Tariq, Z. Zhou, U. Farooq, Z. Abbas, L. Cao, J. Yang, Iridium substitution in nickel cobaltite renders high mass specific OER activity and durability in acidic media, Appl. Catal. B-Environ. 244 (2019) 295–302.

[10] X. Li, Y. Sun, Q. Wu, H. Liu, W. Gu, X. Wang, Z. Cheng, Z. Fu, Y. Lu, Optimized electronic configuration to improve the surface absorption and bulk conductivity for enhanced oxygen evolution reaction, J. Am. Chem. Soc. 141 (2019) 3121–3128.

[11] Y.F. Bu, S. Kim, O. Kwon, Q. Zhong, G. Kim, A composite catalyst based on perovskites for overall water splitting in alkaline conditions, ChemElectroChem 6 (2019) 1520–1524.

[12] Z. Cai, L. Li, Y. Zhang, Z. Yang, J. Yang, Y. Guo, L. Guo, Amorphous nanocages of Cu-Ni-Fe hydr(oxy)oxide prepared by photocorrosion for highly efficient oxygen evolution, Angew. Chem.-Int. Ed. 58 (2019) 4189–4194.

[13] J.-J. Lv, Y. Li, S. Wu, H. Fang, L.-L. Li, R.-B. Song, J. Ma, J.-J. Zhu, Oxygen species on nitrogen-doped carbon nanosheets as efficient active sites for multiple electrocatalysis, ACS Appl. Mater. Interfaces 10 (2018) 11678–11688.

[14] Y. Yang, L. Dang, M.J. Shearer, H. Sheng, W. Li, J. Chen, P. Xiao, Y. Zhang, R.J. Hamers, S. Jin, Highly active trimetallic NiFeCr layered double hydroxide electrocatalysts for oxygen evolution reaction, Adv. Energy Mater. 8 (2018) 1703189.

[15] Y. Pei, Y. Ge, H. Chu, W. Smith, P. Dong, P.M. Ajayan, M. Ye, J. Shen, Controlled synthesis of 3D porous structured cobalt-iron based nanosheets by electrodeposition as asymmetric electrodes for ultra-efficient water splitting, Appl. Catal. B-Environ. 244 (2019) 583–593.

[16] J. Suntivich, K.J. May, H.A. Gasteiger, J.B. Goodenough, Y. Shao-Horn, A perovskite oxide optimized for oxygen evolution catalysis from molecular orbital principles, Science 334 (2011) 1383–1385.

[17] A. Grimaud, K.J. May, C.E. Carlton, Y.-L. Lee, M. Risch, W.T. Hong, J. Zhou, Y. Shao-Horn, Double perovskites as a family of highly active catalysts for oxygen evolution in alkaline solution, Nat. Commun. 4 (2013) 2439.

[18] J.R. Petrie, V.R. Cooper, J.W. Freeland, T.L. Meyer, Z. Zhang, D.A. Lutterman, H.N. Lee, Enhanced bifunctional oxygen catalysis in strained LaNiO3 perovskites, J. Am. Chem. Soc. 138 (2016) 2488–2491.

[19] X. Huang, Double perovskite LaFexNi1-xO3 nanorods enable efficient oxygen evolution electrocatalysis, Angew. Chem. (Int. Ed. Engl.) 58 (2019) 2316–2320.

[20] R.K. Hona, F. Ramezanipour, Remarkable oxygen-evolution activity of a perovskite oxide from the Ca2-xSrxFe2O6-delta, Angew. Chem. (Int. Ed. Engl.) 58 (2019) 2060–2063.

[21] E. Omari, M. Omari, D. Barkat, Oxygen evolution reaction over copper and zinc co-doped LaFeO3 perovskite oxides, Polyhedron 156 (2018) 116–122.

[22] B.-J. Kim, X. Cheng, D.F. Abbott, E. Fabbri, F. Bozza, T. Graule, I.E. Castelli, L. Wiles, N. Danilovic, K.E. Ayers, N. Marzari, T.J. Schmidt, Highly active nano-perovskite catalysts for oxygen evolution reaction: insights into activity and stability of Ba0.5Sr0.5Co0.8Fe0.2O2 + delta and PrBaCo2O5 + delta, Adv. Funct. Mater. 28 (2018) 1804355.

[23] N.-I. Kim, S.-H. Cho, S.H. Park, Y.J. Lee, R.A. Afzal, J. Yoo, Y.-S. Seo, Y.J. Lee, J.-Y. Park, B-Site doping effects of NdBa0.75Ca0.25Co2O5 + delta double perovskite catalysts for oxygen evolution and reduction reactions, J. Mater. Chem. A 6 (2018) 17807–17818.

[24] S. Peng, X. Han, L. Li, S. Chou, D. Ji, H. Huang, Y. Du, J. Liu, S. Ramakrishna, Electronic and defective engineering of electrospun CaMnO3 nanotubes for enhanced oxygen electrocatalysis in rechargeable zinc-air batteries, Adv. Energy Mater. 8 (2018) 1800612.

[25] Y. Tong, J. Wu, P. Chen, H. Liu, W. Chu, C. Wu, Y. Xie, Vibronic superexchange in

double perovskite electrocatalyst for efficient electrocatalytic oxygen evolution, J. Am. Chem. Soc. 140 (2018) 11165–11169.
[26] L. Wang, K.A. Stoerzinger, L. Chang, J. Zhao, Y. Li, C.S. Tang, X. Yin, M.E. Bowden, Z. Yang, H. Guo, L. You, R. Guo, J. Wang, K. Ibrahim, J. Chen, A. Rusydi, J. Wang, S.A. Chambers, Y. Du, Tuning bifunctional oxygen electrocatalysts by changing the A-site rare-earth element in perovskite nickelates, Adv. Funct. Mater. 28 (2018) 1803712.
[27] H. Liu, J. Yu, J. Sunarso, C. Zhou, B. Liu, Y. Shen, W. Zhou, Z. Shao, Mixed protonic-electronic conducting perovskite oxide as a robust oxygen evolution reaction catalyst, Electrochim. Acta 282 (2018) 324–330.
[28] X.M. Xu, Y.L. Pan, W. Zhou, Y.B. Chen, Z.B. Zhang, Z.P. Shao, Toward enhanced oxygen evolution on perovskite oxides synthesized from different approaches: a case study of Ba0.5Sr0.5Co0.8Fe0.2O3-delta, Electrochim. Acta 219 (2016) 553–559.
[29] Y.F. Bu, O. Gwon, G. Nam, H. Jang, S. Kim, Q. Zhong, J. Cho, G. Kim, A highly efficient and robust cation ordered perovskite oxide as a bifunctional catalyst for rechargeable zinc-air batteries, ACS Nano 11 (2017) 11594–11601.
[30] Y. Zhu, W. Zhou, Z.-G. Chen, Y. Chen, C. Su, M.O. Tade, Z. Shao, SrNb0.1Co0.7Fe0.2O3-delta perovskite as a next-generation electrocatalyst for oxygen evolution in alkaline solution, Angew. Chem.-Int. Ed. 54 (2015) 3897–3901.
[31] Y. Zhu, W. Zhou, J. Sunarso, Y. Zhong, Z. Shao, Phosphorus-doped perovskite oxide as highly efficient water oxidation electrocatalyst in alkaline solution, Adv. Funct. Mater. 26 (2016) 5862–5872.
[32] Y. Guo, Y. Tong, P. Chen, K. Xu, J. Zhao, Y. Lin, W. Chu, Z. Peng, C. Wu, Y. Xie, Engineering the electronic state of a perovskite electrocatalyst for synergistically enhanced oxygen evolution reaction, Adv. Mater. 27 (2015) 5989–5994.
[33] X. Xu, C. Su, W. Zhou, Y. Zhu, Y. Chen, Z. Shao, Co-doping strategy for developing perovskite oxides as highly efficient electrocatalysts for oxygen evolution reaction, Adv. Sci. 3 (2016) 1500187.
[34] X. Xu, Y. Chen, W. Zhou, Y. Zhong, D. Guan, Z. Shao, Earth-abundant silicon for facilitating water oxidation over iron-based perovskite electrocatalyst, Adv. Mater. Interfaces 5 (2018) 1701693.
[35] Y. Zhu, W. Zhou, Z. Shao, Perovskite/carbon composites: applications in oxygen electrocatalysis, Small 13 (2017) 1603793.
[36] Y. Bu, G. Nam, S. Kim, K. Choi, Q. Zhong, J. Lee, Y. Qin, J. Cho, G. Kim, A tailored bifunctional electrocatalyst: boosting oxygen reduction/evolution catalysis via electron transfer between N-doped graphene and perovskite oxides, Small 14 (2018) 1802767.
[37] Y. Bu, H. Jang, O. Gwon, S.H. Kim, S.H. Joo, G. Nam, S. Kim, Y. Qin, Q. Zhong, S.K. Kwak, J. Cho, G. Kim, Synergistic interaction of perovskite oxides and N-doped graphene in versatile electrocatalyst, J. Mater. Chem. A 7 (2019) 2048–2054.
[38] Z. Chen, A. Yu, D. Higgins, H. Li, H. Wang, Z. Chen, Highly active and durable core-corona structured bifunctional catalyst for rechargeable metal-air battery application, Nano Lett. 12 (2012) 1946–1952.
[39] M. Zhao, J. Zhang, H. Xiao, T. Hu, J. Jia, H. Wu, Facile in situ synthesis of a carbon quantum dot/graphene heterostructure as an efficient metal-free electrocatalyst for overall water splitting, Chem. Commun. 55 (2019) 1635–1638.
[40] D. Tang, J. Liu, X. Wu, R. Liu, X. Han, Y. Han, H. Huang, Y. Liu, Z. Kang, Carbon quantum dot/NiFe layered double-hydroxide composite as a highly efficient electrocatalyst for water oxidation, ACS Appl. Mater. Interfaces 6 (2014) 7918–7925.
[41] P. Zhang, T. Song, T. Wang, H. Zeng, In-situ synthesis of Cu nanoparticles hybridized with carbon quantum dots as a broad spectrum photocatalyst for improvement of photocatalytic H-2 evolution, Appl. Catal. B-Environ. 206 (2017) 328–335.
[42] Z. Zhang, B. He, L. Chen, H. Wang, R. Wang, L. Zhao, Y. Gong, Boosting overall water splitting via FeOOH nanoflake-decorated PrBa0.5Sr0.5Co2O5 + delta nanorods, ACS Appl. Mater. Interfaces 10 (2018) 38032–38041.
[43] S.P. Mukherjee, A.R. Gliga, B. Lazzaretto, B. Brandner, M. Fielden, C. Vogt, L. Newman, A.F. Rodrigues, W. Shao, P.M. Fournier, M.S. Toprak, A. Star, K. Kostarelos, K. Bhattacharya, B. Fadeel, Graphene oxide is degraded by neutrophils and the degradation products are non-genotoxic, Nanoscale 10 (2018) 1180–1188.
[44] D. Chao, C. Zhu, X. Xia, J. Liu, X. Zhang, J. Wang, P. Liang, J. Lin, H. Zhang, Z.X. Shen, H.J. Fan, Graphene quantum dots coated VO2 arrays for highly durable electrodes for Li and Na ion batteries, Nano Lett. 15 (2015) 565–573.
[45] L. Gui, Y. Chen, B. He, G. Li, J. Xu, Q. Wang, W. Sun, L. Zhao, Nickel-based bicarbonates as bifunctional catalysts for oxygen evolution and reduction reaction in alkaline media, Chem. A Eur. J. 24 (2018) 17665–17671.
[46] S. Zhao, C. Li, L. Wang, N. Liu, S. Qiao, B. Liu, H. Huang, Y. Liu, Z. Kang, Carbon quantum dots modified MoS2 with visible-light-induced high hydrogen evolution catalytic ability, Carbon 99 (2016) 599–606.
[47] H. Hu, L. Gui, W. Zhou, J. Sun, J. Xu, Q. Wang, B. He, L. Zhao, Partially reduced Sn/SnO2 porous hollow fiber: a highly selective, efficient and robust electrocatalyst towards carbon dioxide reduction, Electrochim. Acta 285 (2018) 70–77.
[48] Y. Matsumoto, E. Sato, Electrocatalytic properties of transition-metal oxides for oxygen evolution reaction, Mater. Chem. Phys. 14 (1986) 397–426.
[49] P.P. Gao, X.K. Tian, Y.L. Nie, C. Yang, Z.X. Zhou, Y.X. Wang, Promoted peroxymonosulfate activation into singlet oxygen over perovskite for ofloxacin degradation by controlling the oxygen defect concentration, Chem. Eng. J. 359 (2019) 828–839.
[50] X. Xu, Y. Chen, W. Zhou, Z. Zhu, C. Su, M. Liu, Z. Shao, A perovskite electrocatalyst for efficient hydrogen evolution reaction, Adv. Mater. 28 (2016) 6442–6448.
[51] C.F. Chen, G. King, R.M. Dickerson, P.A. Papin, S. Gupta, W.R. Kellogg, W. Gang, Oxygen-deficient BaTiO3 − x perovskite as an efficient bifunctional oxygen electrocatalyst, Nano Energy 13 (2015) 423–432.
[52] R. Liu, F. Liang, Z. Wei, Y. Yang, Z. Zhu, Calcium-doped lanthanum nickelate layered perovskite and nickel oxide nano-hybrid for highly efficient water oxidation, Nano Energy 12 (2015) 115–122.
[53] I.C. Man, H.Y. Su, F. Calle-Vallejo, H.A. Hansen, J.I. Martinez, N.G. Inoglu, J. Kitchin, T.F. Jaramillo, J.K. Norskov, J. Rossmeisl, Universality in oxygen evolution electrocatalysis on oxide surfaces, ChemCatChem 3 (2011) 1159–1165.
[54] N.I. Kim, S.H. Cho, S.H. Park, Y.J. Lee, R.A. Afzal, J. Yoo, Y.S. Seo, Y.J. Lee, J.Y. Park, B-Site doping effects of NdBa0.75Ca0.25Co2O5 + delta double perovskite catalysts for oxygen evolution and reduction reactions, J. Mater. Chem. A 6 (2018) 17807–17818.
[55] X. Han, C. Yu, S. Zhou, C. Zhao, H. Huang, J. Yang, Z. Liu, J. Zhao, J. Qiu, Ultrasensitive iron-triggered nanosized Fe-CoOOH integrated with graphene for highly efficient oxygen evolution, Adv. Energy Mater. 7 (2017) 1602148.
[56] S.-H. Ye, Z.-X. Shi, J.-X. Feng, Y.-X. Tong, G.-R. Li, Activating CoOOH porous nanosheet arrays by partial iron substitution for efficient oxygen evolution reaction, Angew. Chem.-Int. Ed. 57 (2018) 2672–2676.
[57] Y. Zhu, W. Zhou, Y. Zhong, Y. Bu, X. Chen, Q. Zhong, M. Liu, Z. Shao, A perovskite nanorod as bifunctional electrocatalyst for overall water splitting, Adv. Energy Mater. 7 (2017) 1602122.
[58] J. Wang, Y. Gao, D. Chen, J. Liu, Z. Zhang, Z. Shao, F. Ciucci, Water splitting with an enhanced bifunctional double perovskite, ACS Catal. 8 (2018) 364–371.
[59] B. Hua, M. Li, Y.-F. Sun, Y.-Q. Zhang, N. Yan, J. Chen, T. Thundat, J. Li, J.-L. Luo, A coupling for success: controlled growth of Co/CoOx nanoshoots on perovskite mesoporous nanofibres as high-performance trifunctional electrocatalysts in alkaline condition, Nano Energy 32 (2017) 247–254.
[60] B. Hua, M. Li, J.-L. Luo, A facile surface chemistry approach to bifunctional excellence for perovskite electrocatalysis, Nano Energy 49 (2018) 117–125.
[61] B. Hua, L. Meng, Y.Q. Zhang, Y.F. Sun, J.L. Luo, All-in-one perovskite catalyst: smart controls of architecture and composition toward enhanced oxygen/hydrogen evolution reactions, Adv. Energy Mater. 7 (2017) 1700666.